Journal of Structural Biology 218 (2026) 108313

Contents lists available at ScienceDirect

Journal of Structural Biology

journal homepage: www.elsevier.com/locate/yjsbi

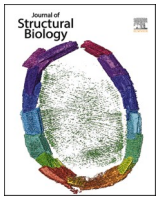

Research Article

Leveraging deep learning semantic segmentation for imaging coral skeletons

Alejandra Coronel-Zegarra [a], Jamie L. Knaub [b], Vivian Merk [a,*], Abhijit Pandya [c]

[a] Department of Chemistry and Biochemistry, Department of Ocean and Mechanical Engineering, Florida Atlantic University, Boca Raton, FL 33431, the United States of America
[b] FAU Lab Schools, Florida Atlantic University, Boca Raton, FL 33431, the United States of America
[c] Department of Electrical Engineering and Computer Science, Department of Biomedical Engineering, Florida Atlantic University, Boca Raton, FL 33431, the United States of America

ARTICLE INFO

Keywords:
X-ray tomography
Deep learning
Image segmentation
Convolutional neural networks
Biomineral
Morphogenesis

ABSTRACT

Micro-computed tomography and semantic segmentation provide insights into the structural hierarchy of biomineralized tissues, as exemplified by stony coral skeletons. Non-destructive imaging reveals mechanistic aspects of skeletal growth, including variations in porosity, density, and skeletal thickness across species and in the context of disease. Recent developments in semantic segmentation based on convolutional neural network models are poised to transform the streamlined analysis of large 3D tomography datasets, surpassing the performance of traditional segmentation methods. In this work, a series of U-Net deep learning models were trained and applied on exemplary micro-CT datasets from stony corals pertaining to *Montastraea cavernosa* and *Porites astreoides* species for the segmentation of pores and skeleton. The models were statistically evaluated, revealing that Attention U-Net was the top performer with respect to computational efficiency, accuracy, and generalizability, followed by U-Net++ and standard U-Net. Our analysis highlights accuracy limitations of U-Net-based deep learning segmentations that can result in false-positive or false-negative classifications. The segmented 3D models were utilized to perform porosity, bulk density, and thickness analyses of each dataset, revealing quantitative differences between the two species, as well as between healthy and stony coral tissue loss disease afflicted *M. cavernosa* coral skeletons. This work provides a framework for streamlined training and deployment of deep learning models for semantic segmentation of calcified tissues that inform our understanding of skeletogenesis and growth patterns across species and pathogenesis contexts.

1. Introduction

Semantic image segmentation is a popular technique that involves assigning semantic labels to pixels of images and has been revolutionary in the fields of medical imaging and materials science Davydzenka et al., 2022; Wang et al., 2022). In materials science, the use of non-destructive X-ray imaging and image segmentation has facilitated the characterization of internal micro- and nanostructures, such as phase and grain boundaries, voids or cracks. For example, image segmentation has proven to be a useful tool for studying the interplay between nanoscale grain size and mechanical performance of metals or alloys in industrial settings (Dursun & Soutis, 2014; Hu et al., 2017). However, studying biological materials using X-ray tomography and image segmentation presents challenges due to complex and overlapping micro- and nanostructures, noisy image conditions, and low contrast (Duke et al., 2017). Despite this, complex biological materials have traditionally been evaluated by manual image segmentation (Dai et al., 2013; Darrow et al., 2015; Wang et al., 2015).

Micro-computed tomography (micro-CT) is an imaging technique that uses X-rays to resolve internal three-dimensional (3D) structures at a (sub)micron level (Vásárhelyi et al., 2020). With respect to materials characterization, micro-CT can be a powerful tool for determining qualitative and quantitative information such as porosity, pore size and shape distribution, tortuosity, thickness distribution, phase fractions, phase contiguity, and orientation (Maire & Withers, 2014). For instance, micro-CT has been used to study bone penetration into solid implants, proving to be a viable approach to evaluate the performance and incorporation of biomaterials (Cohen et al., 2017). A recent study

* Corresponding author.
E-mail address: vmerk@fau.edu (V. Merk).

https://doi.org/10.1016/j.jsb.2026.108313
Received 11 September 2025; Received in revised form 5 March 2026; Accepted 9 March 2026
Available online 10 March 2026

developed bio-inspired micro air vehicles based on tomographic reconstructions of fly wings (Rubio & Chakravarty, 2016).

X-ray tomography has been extensively used to elucidate the microstructure, growth mechanism, and preferred orientation of biomineralized systems found in exo- and endoskeletons and other hard tissues of living organisms (Furat et al., 2019; Reznikov et al., 2020). An example of biomineralized structures in the marine environment are scleractinian corals, which primarily build their skeletons from a biomineral called aragonite, a highly ordered polymorph of calcium carbonate ($CaCO_3$) (San et al., 2022). Studies on coral skeletons have provided insights into morphological changes related to environmental stressors (Thompson, 2022) and overall coral health (Lough & Cooper, 2011). Micro-CT imaging has been leveraged to study skeletal growth, including the impact of ecological and environmental factors on growth direction, bulk density, and calcification rates (Fouke et al., 2021). For example, micro-CT has been used to compare skeletal features and canal systems in various reef-building coral species, suggesting species-specific growth patterns and colony pattern regulations of dominant reef-building corals (Li et al., 2021). Similarly, fluctuations in environmental conditions result in seasonal banding patterns in massive scleractinian corals, as shown by X-ray imaging and image segmentation (Vincent & Sheldrake, 2025). Thus, micro-CT can serve as a powerful tool for systematically analyzing complex aspects of coral biomineralization that are not yet fully understood, such as the effects on environmental stressors and disease on skeletal growth mechanisms. This work attempts to leverage deep learning-based image segmentations of coral micro-CT data using an extensive model evaluation and selection framework to streamline porosity analyses of different coral species, as well as healthy and diseased corals.

Due to their high mineral content, coral skeletons are characterized by a high X-ray absorption coefficient, rendering them ideal samples for X-ray imaging. Various studies harnessed micro-CT techniques to investigate healthy coralline skeletons, particularly focusing on seasonal porosity fluctuations or growth bandings. Moreover, image segmentation studies of coral micro-CT data have investigated the effects of ocean acidification (Scucchia et al., 2022, 2025) and acclimatory abilities (Scucchia et al., 2023) with respect to skeletal thickness and porosity. However, little is known about how common coral diseases (e.g., Blackband Disease, Stony Coral Tissue Loss Disease, or Aspergillosis) may affect skeletal patterns and microstructure. Specifically, the use of deep learning assisted semantic segmentation remains underexplored in the field of biomaterials. Previous studies on the stony coral species *Porites compressa* tied skeletal growth anomalies in diseased corals to high porosity (Domart-Coulon et al., 2006; Andersson et al., 2020). Scucchia *et al.* applied the U-Net network architecture algorithm to segment rapid accretion deposits (RADs, also known as centers of calcification) and thickening deposits (TDs) in coral skeletons (Domart-Coulon et al., 2006).

While sample preparation protocols and tomography scan parameters should be optimized, some experimental settings are associated with sub-optimal data collection, such as inline quality control in industry or in-situ experiments at synchrotron beamlines. Even under the assumption of high-quality data collection, deep learning image segmentation techniques may provide unique advantages by accelerating and streamlining data analysis. In some cases, manual segmentation proves impossible since minor grey value variations cannot be discerned by eye.

In this study, modern deep learning image segmentation tools were tested and evaluated to automatically identify and delineate skeletal features. State-of-the-art image segmentation tools are crucial for accelerating materials characterization and quantitative analysis, enabling high-throughput analysis, and improving accuracy and reproducibility. In recent years, deep learning-based image segmentation algorithms have grown in popularity due to their exceptional performance compared to traditional segmentation methods (Minaee et al., 2022). Specifically, convolutional neural networks (CNNs) have been widely used for image segmentation tasks (Fukushima, 1980; Lecun et al., 1998; Waibel et al., 1989). The use of convolution layers provides the advantage of enhanced feature extraction, while nonlinear layers provide robustness through the ability to model nonlinear functions (Maire & Withers, 2014). In addition, pooling layers reduce dimensionality of input images for efficient memory usage. Up to our knowledge, only few studies have systematically compared deep-learning image segmentations of X-ray tomography reconstructions from biomineralized materials based on performance metrics and statistical evaluations.

A popular CNN-based deep learning network, U-Net, has excelled specifically for biomedical image segmentation (Ronneberger et al., 2015). Developed by Ronneberger *et al*, U-Net assumes an encoder-decoder structure consisting of a contracting and expansive path (Fig. 1). The contracting path assumes a typical architecture of a CNN, with repeated doublets of 3x3 convolutions, followed by a rectified linear unit (ReLU) and a 2x2 max pooling layer. The contracting path essentially consists of "downsampling" steps. The expansive path consists of an "upsampling" step followed by a 2x2 convolution and a doublet of 3x3 convolutions, each followed again by a ReLU. A final 1x1 convolution is then applied to map each component feature vector corresponding to the number of classes.

Notably, the use of skip connections in the U-Net architecture have allowed for recovery of fine-grained details even with complex backgrounds. Nonetheless, to meet the strict demands of segmenting medical images, variations of U-Net were created to address its shortcomings in this regard. U-Net++, introduced by Zhou *et al,* is an encoder-decoder network where the subnetworks are connected by nested, dense skip connections in order to reduce the semantic gap between feature maps of each sub-network (Zhou et al., 2018). Another variation is Attention U-Net, which adds an attention gate (AG) model to eliminate the need for additional supervision while focusing on target structures of varying sizes and shapes (Oktay et al., 2018).

While these networks have been created and optimized for medical imaging segmentations, they have found wide-spread application in materials, earth, and life science applications as well. For instance, the skeletal morphology of marine Acantharia has been resolved using synchrotron X-ray nanotomography and U-Net segmentation models (Raja Somu et al., 2023). In geosciences, neural network algorithms have been applied in the tomographic analysis of micro-porous granodiorite rocks (Roslin et al., 2022). Similarly, manufactured aluminum alloys have been visualized using micro-CT, employing U-Net models for porosity and density determinations under tensile stress (Zhang et al., 2023). U-Net models have been employed for studying the morphology of marine bivalve skeletons (Edie et al., 2023). Another study involving deep learning image segmentation revealed nanostructural features in shark vertebral cartilage (Raja Somu et al., 2025). Thus, these models have proven to be viable tools for deep learning micro-CT image segmentations of skeletal systems and biomineralized tissues.

The present study focused on reef-building scleractinian coral species *Montastraea cavernosa* (*M. cavernosa*), which has moderate susceptibility to Stony Coral Tissue Loss Disease (SCTLD) (Papke et al., 2023), an aggressive coral disease that emerged in 2014 and has decimated entire coral colonies across Florida and the Caribbean over the last few years (Alvarez-Filip et al., 2022). Another species, *Porites astreoides* (*P. atreoides*), which has commonly been used in micro-CT studies, was also included to diversify the datasets used for testing the U-Net models. Herein, we investigated micro-CT reconstructions of *M. cavernosa*, including healthy and SCTLD-afflicted bulk sections, and *P. astreoides* to investigate differences in porosity and pore size distributions using deep learning image segmentation algorithms. Micro-CT datasets were acquired in standard absorption mode using a laboratory-source micro-CT scanner. U-Net models were employed and evaluated in a comparative performance study. Upon evaluation, the models were then used to generate labeled image stacks for subsequent skeletal porosity, density, and thickness analyses. The top performing model, Attention U-Net was used to generate labeled image stacks for subsequent porosity analyses. Overall, this work aims to evaluate the performance of deep learning

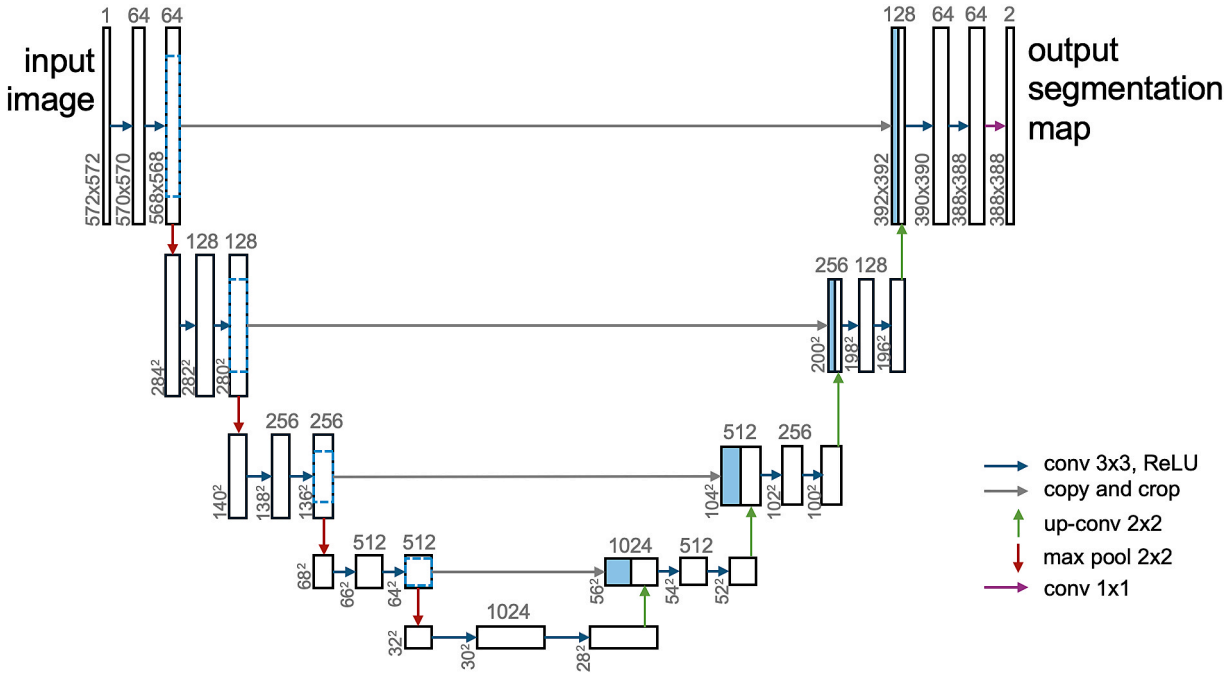

Fig. 1. Adapted U-Net architecture (Ronneberger et al., 2015).

image segmentations compared to traditional manual labeling methods, like histogram-based thresholding, to derive quantitative parameters (e.g., porosity) of healthy and SCTLD-afflicted corals.

2. Methodologies

2.1. Coral sample preparation

Healthy and SCTLD infected *Montastraea cavernosa (M. cavernosa)* coral samples were collected by technical diving from the northwestern Atlantic Ocean, offshore from Pompano Beach, FL. Samples were washed by hand with DI water to remove excess organic tissue and air dried for 48 h. The large section of diseased *M. cavernosa* coral (MCAV_SCTLD1) was cut into 20 mm × 10 mm × 6 mm section using a Buehler Isomet 1000 diamond precision saw. The smaller section of diseased coral (MCAV_SCTLD2) was cut into 6 mm × 8 mm × 1.5 mm section using a Buehler Isomet 1000 diamond precision saw. The healthy *M. cavernosa* (MCAV_healthy) and *Porites astreoides* (PAST) sections were used without further modifications.

2.2. Micro-computed tomography scanning (Micro-CT)

Coral samples were imaged with a Bruker SkyScan 1173 system (Kontich, Belgium) in the Berlin Family Bioimaging Lab at FAU Lab Schools Marcus Research and Innovation Center (RRID:SCR_023805). Scan acquisition settings included a flatfield correction, 3x frame averaging, and 0.2-degree rotation step. The MCAV_SCTLD2 sample was scanned at 90 kV (voltage), 88μA (current), 615 ms exposure, with a voxel size of 5.51 μm, and without X-ray filtering. All other samples were scanned at 120 kV, 60 μA, 700 ms exposure, with a voxel size between 15.14–17.46 μm and 1.0 mm aluminum filter (Table 1). Radiographs (16-bit TIFFs) were reconstructed using the Bruker NRecon (Version 1.7.1.0) software with 15% beam hardening correction and 5–10 (scan dependent) ring artifact correction. 3D volume renderings were then created using Dragonfly's 3D tools (Fig. 2) (Comet Technologies Canada Inc., n.d.). The resulting datasets consisted of 1200–1400 2D projections sliced beginning at the basal body plate of the sample past the newest growth at the top of the corallite. Due to the large size of the samples, image stacks were cropped to exclude surrounding airspace, while still preserving an adequate surface of the sample for segmentation of classes. The resulting datasets are summarized in Table 1.

Table 1
Characteristics of the micro-CT datasets.

Dataset	Width (px)	Height (px)	Depth (px)	Voxel Size (μm)
MCAV_healthy	1257	1293	801	15.14
MCAV_SCTLD1	581	876	446	15.14
MCAV_SCTLD2	949	870	175	5.51
PAST	877	1060	896	17.46

2.3. Ground truth labels (otsu thresholding)

Ground truth labels for each image of the cropped datasets were created on Dragonfly using Otsu Histogram Thresholding (Otsu, 1979). Upper Otsu intensity values were assigned to voxels representing the skeleton of the coral sample. Lower Otsu values were assigned to voxels representing the pores of the sample.

2.4. Training data for segmentation

The training dataset was composed of 200 labeled slices for the MCAV_healthy cropped dataset that adequately represented any variations in the data. This training dataset was used as input into the Deep Learning tool, which separated into training and validation sets at an 80:20 ratio. The training parameters were optimized after multiple runs to those reported in Table 2. Data augmentations were applied on the input data to artificially diversify and increase the dataset to enhance model robustness and generalizability down the road. Augmentations included vertical and horizontal flip transformations, 180° rotations, zooming, and shearing.

2.5. Deployment of trained models

After each model was successfully trained, it was applied to the entire datasets. The resulting images with predicted labels were generated from scalar values of voxel count for each class and exported as image stacks for performance computations. The image stacks were

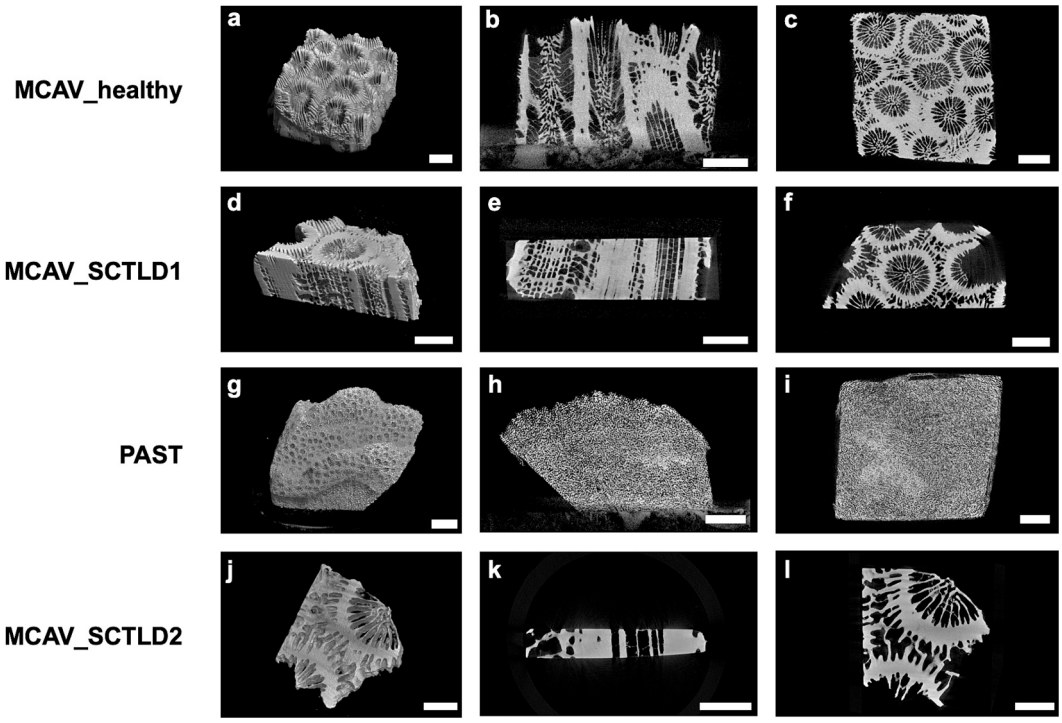

Fig. 2. Visual representations of micro-CT 3D reconstructions of coral sections used in the study. 3D renderings (a, d, g, j), side view (b, e, h, k), and top view (c, f, i, l) of healthy *M. cavernosa* coral section (MCAV_healthy), large SCTLD-afflicted *M. cavernosa* coral section (MCAV_SCTLD1), healthy *P. astreoides* coral section (PAST) and smaller SCTLD-afflicted *M. cavernosa* coral section (MCAV_SCTLD2), respectively. Scale bars correspond to 5 mm (a-i) and 2 mm (j-l).

Table 2
Model parameters for all U-Net models.

Standardized model parameters	
Class count	2
Depth level	5
Initial filter count	64
Patch Size	[64, 64, 1]
Stride Ratio	1
Batch size	32
Epochs number	100
Loss function	Categorical Cross-entropy
Optimization algorithm	Adadelta
Metrics	Categorical accuracy, loss
Training/Validation	80/20

binarized for subsequent calculations of true positive (TP), false positive (FP), true negative (TN), and false negative (FN) values based on voxel counts. Using these values, performance metrics like accuracy, recall, precision, F1-score, false positive rate (FPR), true negative rate (TNR), and false negative rate (FNR) were calculated to further evaluate the models.

2.6. Statistical tests

Slice-wise accuracies were compiled and used as the representative metric for each test in R Studio. Performance evaluations were conducted using a Two-Way Analysis of Variance (ANOVA) test to determine statistical differences in mean slice-wise accuracies for the three models on all datasets. A Tukey's Honestly Significant Difference (HSD) test was run post-hoc from the ANOVA results to determine which group means differed significantly in a pairwise comparison for the three models.

2.7. Porosity & bulk density calculations

Porosity calculations were performed using segmented binarized image slices from all three models as well as the ground truth labeled images. Before computations, image stacks for each dataset were examined for incomplete slices at the top and bottom of a stack, which did not encompass the full segmented area due to uneven sample surfaces (Fig. S1). These slices were removed from the stack for the following calculations to prevent inaccuracies. Slice-wise porosity profiles (ϕ) were computed by pixel count of pores over total pixels per 2D image. Bulk density values were computed by first assuming the known density of aragonite ($\rho_{aragonite}$) as 2.94 g/cm^3 (Zhong et al., 2024). The following equation was then used to calculate bulk densities per image slice.

$$\rho_{bulk} = \rho_{aragonite} * (1 - \phi)$$

Depth values in mm were computed by converting depth (z) values of each slice from pixel to mm using image voxel sizes corresponding to each dataset. Porosity profiles, bulk density values, and depths in mm for each image slice were stored and used to visualize porosity and bulk density across the depth of each sample.

2.8. Thickness mesh generation

Thickness meshes were created for MCAV_healthy, PAST, and MCAV_SCTLD1 samples using Dragonfly's Thickness Mesh tool of the skeleton class from all predicted and ground truth segmentations. This tool works by computing diameters of hypothetical spheres that fit within boundary points to generate color-boded meshes of local thickness values between these boundary points. The MCAV_SCLTD2 dataset was excluded due to the small vertical profile related to the depth of the sample, which prevented visualization of skeletal thickness across an adequate length scale.

3. Results & discussion

3.1. U-Net models for semantic segmentations

Micro-CT images of both the healthy and SCTLD-afflicted corals were trained and tested using a series of U-Net models to evaluate segmentation performance for a binary classification (Fig. 3). Training results are summarized in Table 3. All three models showed good performance during training, with upwards of 98% accuracy and dice coefficient scores. The U-Net model was trained in the least number of epochs, followed by the Attention U-Net and U-Net++. In terms of training times, Attention U-Net took roughly 7 h, which was significantly faster than U-Net at 15 h and U-Net++ at 17 h. Comparison of training and validation accuracy and loss revealed consistent trends of higher validation accuracy and lower validation loss for all models (Fig. 4, Table 3), indicative of sufficiently trained models.

Table 3
Performance metrics for all U-Net models after training.

Model	No. epochs trained	Model accuracy	Model loss	Model dice coefficient
U-Net	38	0.9955	0.00969	0.9925
U-Net++	76	0.9888	0.02446	0.9835
Attention U-Net	48	0.9870	0.02821	0.9809

Deployment of the models would verify their classification performance and generalizability. Performance metrics for each model on

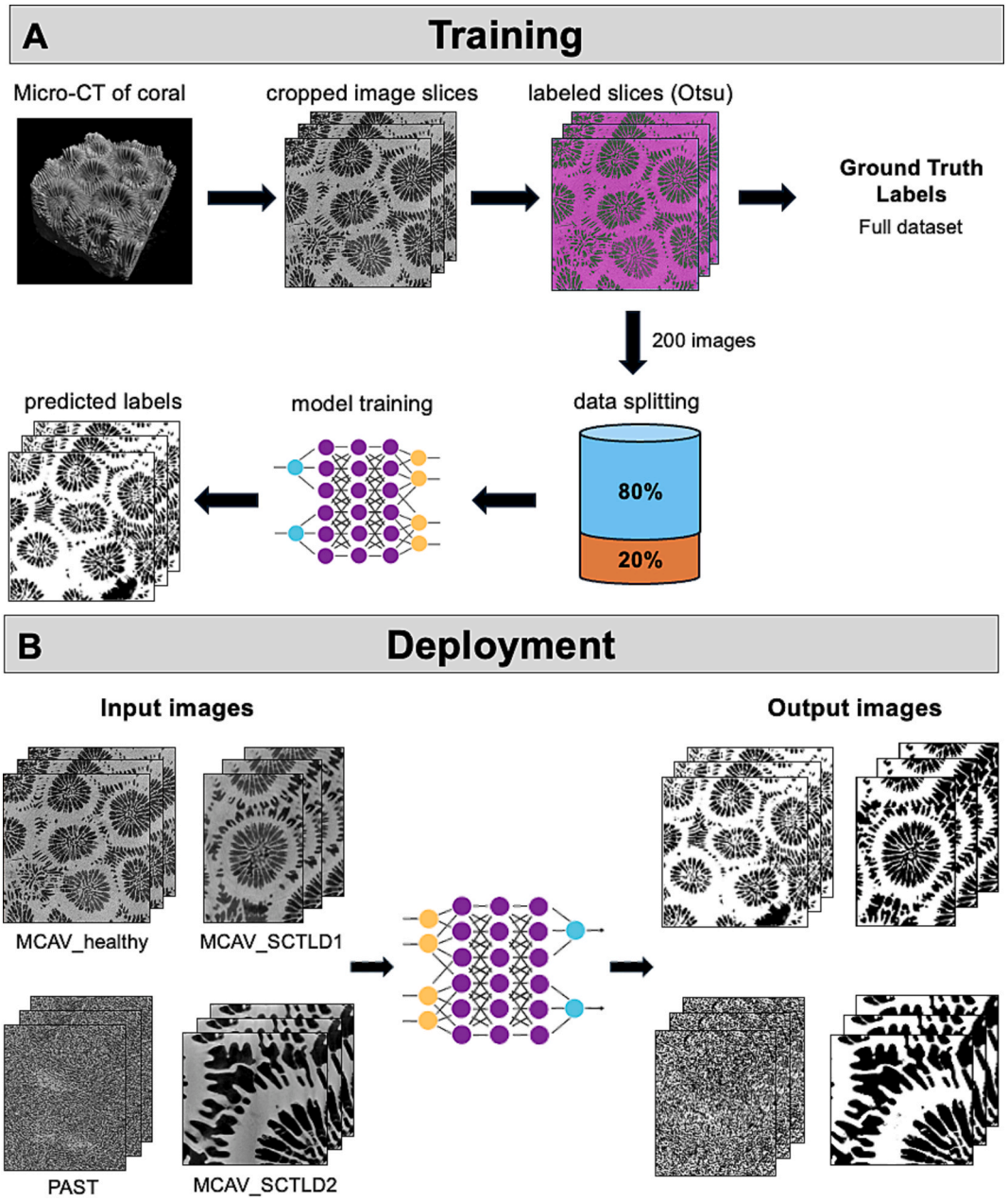

Fig. 3. (A) Training workflow; reconstructed micro-CT image slices were cropped and labeled using Otsu thresholding, forming the ground truth labels (pore and skeleton). A portion of those labeled images were allocated to train the models. The images were split into training and validation and inputted into the models for training. The predicted labels were outputted, verifying successful training of the models. (B) Deployment workflow; the trained models were then applied to the full datasets of both healthy and diseased coral micro-CT images, which were inputted into the models. The models outputted the image stacks with prediction labels for the two classes (pore and skeleton).

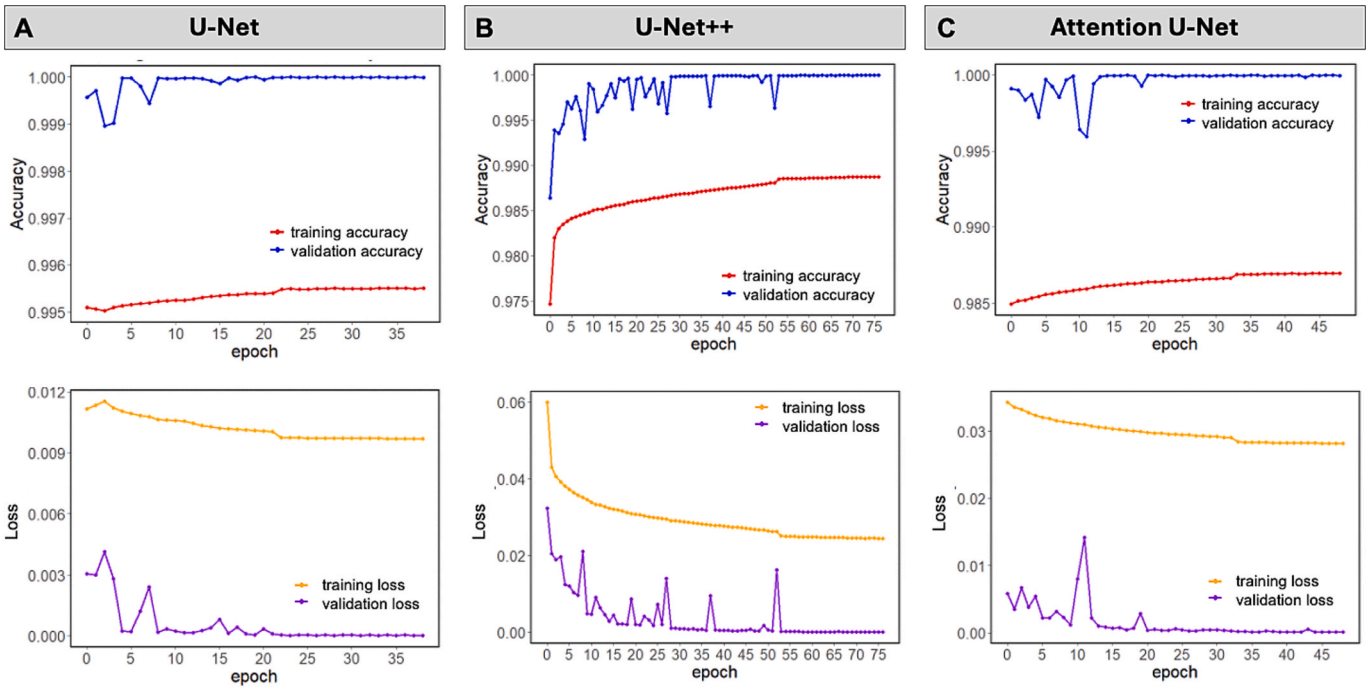

Fig. 4. Accuracy and Loss plot during training and validation for (A) U-Net, (B) U-Net++, and (C) Attention U-Net.

each dataset were computed and are summarized in Table 4. Confusion matrices were compiled for each model on both datasets using TP, FP, TN, FN values (Fig. 5). All models achieved segmentation accuracy scores over 89%, highlighting weaknesses in currently used segmentation approaches resulting from false-positive or false-negative classifications. Despite having the highest accuracy during training, the U-Net standard model had the lowest average accuracy when applied to unseen data. This could suggest possible overfitting during training. U-Net exhibited lower precision scores, especially for the PAST dataset, meaning there were more voxels mislabeled as skeleton (false positives) compared to the other two models. This is especially evident when comparing ground truth-labeled image slices (Fig. 6a) with image slices with prediction labels from U-Net (Fig. 6b). The F1-Scores were also the lowest overall amongst the three models.

Similarly, despite the U-Net model having a recall of 1.0, meaning correct prediction of skeletal structures, this was at the expense of higher FPR values of around 13–16%. U-Net overall performs relatively well but not competitively compared to the other two models. Being a widely used model in biomedical image segmentation, U-Net has proven to be highly sensitive, but a lack of precision may make it prone to over-segmentation.

Attention U-Net and U-Net++ achieved the best performances overall. U-Net++ had an average accuracy across all datasets of about 95% and a high precision of around 1.0 across datasets. While accuracies and F1-scores were high for the MCAV_healthy and MCAV_SCTLD1 datasets, performance dropped in MCAV_SCTLD2 and PAST datasets, especially in recall and F1-Score. Nonetheless, its performance on PAST was only slightly worse than MCAV_healthy and MCAV_SCTLD1, as shown by their predicted labels (Fig. 6c) which matched well with the ground truth labels from Otsu thresholding (Fig. 6a). However, U-Net++ had the worst performance on the MCAV_SCTLD2 dataset, with an 18.9% FNR, meaning that it mislabeled almost 20% of the skeleton voxels as pores. This is evident in a representative MCAV_SCTLD2 image slice with the U-Net++ predicted labels (Fig. 6c). Attention U-Net exhibited similar trends in performance. It had the highest average accuracy for all datasets at 96.6%, as well as the highest F-1 Score in every

Table 4
Performance metrics for each model on all datasets after testing.

	Accuracy	Precision	Recall	F1-Score	TNR	FPR	FNR
U-Net							
MCAV_healthy	0.9465	0.9193	1.0000	0.9579	0.8628	0.1372	0.0000
MCAV_SCTLD1	0.9430	0.9115	1.0000	0.9537	0.8620	0.1380	0.0000
MCAV_SCTLD2	0.9819	1.0000	0.9679	0.9837	1.0000	0.0000	0.0321
PAST	0.9019	0.8049	1.0000	0.8919	0.8358	0.1647	0.0000
U-Net++							
MCAV_healthy	0.9864	0.9999	0.9776	0.9887	1.0000	0.0000	0.0224
MCAV_SCTLD1	0.9913	0.9994	0.9858	0.9925	0.9991	0.0009	0.0142
MCAV_SCTLD2	0.8935	1.0000	0.8110	0.8957	1.0000	0.0000	0.1890
PAST	0.9552	0.9991	0.8901	0.9415	0.9994	0.0006	0.1099
Attention U-Net							
MCAV_healthy	0.9863	0.9999	0.9776	0.9887	1.0000	0.0000	0.0224
MCAV_SCTLD1	0.9914	0.9995	0.9859	0.9927	0.9993	0.0007	0.0141
MCAV_SCTLD2	0.8949	1.0000	0.8135	0.8971	1.0000	0.0000	0.1865
PAST	0.9953	0.9998	0.8898	0.9416	0.9999	0.0001	0.1102

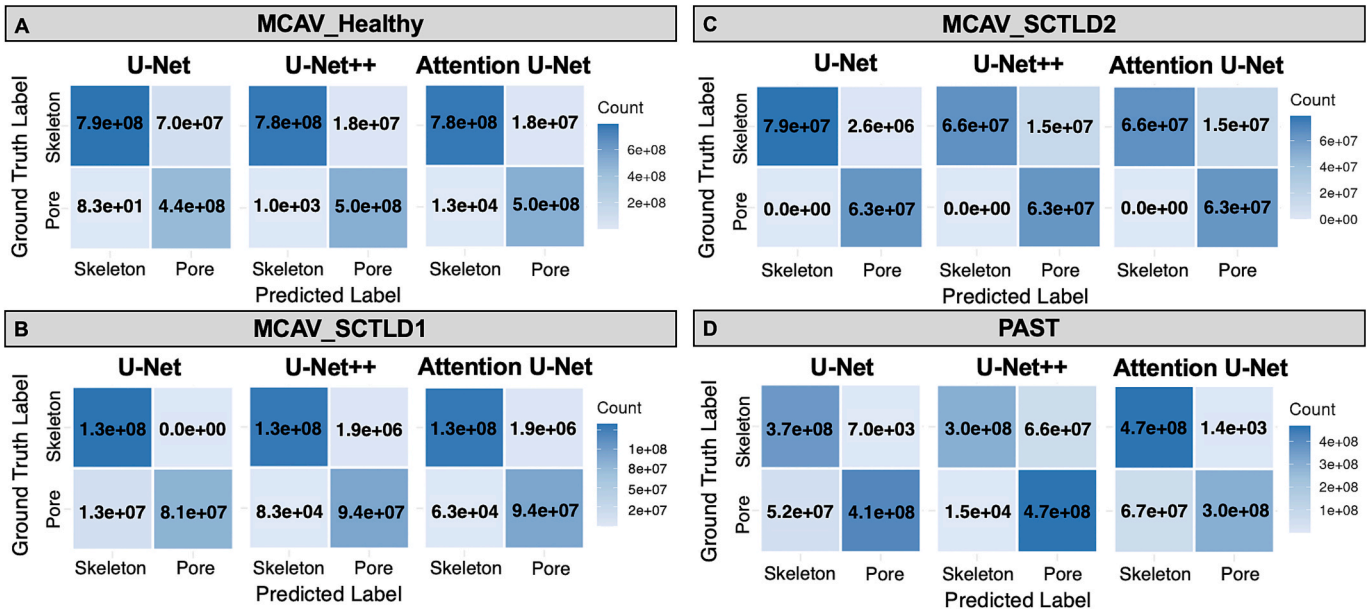

Fig. 5. Confusion matrices for all three models on (A) MCAV_Healthy, (B) MCAV_SCTLD1, (C) MCAV_SCTLD2 and (D) PAST datasets. Values are expressed in voxel counts for each class.

dataset. Precision was high at around 1.0. The Attention U-Net predicted labels (Fig. 6d) for most datasets matched extremely well with the ground truth labels (Fig. 6a). Performance did drop for the MCAV-SCTLD2 dataset, similar to U-Net++, especially in mislabeling skeleton voxels as pore (Fig. 6d). Nonetheless, Attention U-Net had the lowest FPR and FNR rates overall and performed impressively well on the PAST dataset. It had the highest accuracy for the PAST dataset, segmenting skeleton and pores within images of a completely different, more complex pore network than what it was trained on.

Interestingly, U-Net had the best performance metrics for the MCAV_SCTLD2 dataset and the worst performance for the PAST dataset. Attention U-Net and U-Net++ performed very well on the PAST dataset but had the worst metrics for MCAV_SCTLD2. All models were trained only on labeled image slices from the MCAV_healthy dataset. The MCAV_SCTLD1 dataset was the most similar to MCAV_healthy, with the same voxel size and larger surface areas in the images of the same species of coral (*M. cavernosa)*. This would explain why MCAV_healthy and MCAV_SCTLD1 performed the best out of all the datasets for all models. PAST consisted of micro-CT reconstructions of a different stony coral species, *P. astreoides*, with a larger voxel size and a completely distinct pore network compared to the *M. cavernosa.* MCAV_SCTLD2 contained images of a smaller volume of coral with a smaller image voxel size than the rest of the datasets. U-Net may have overfit or failed to generalize on the PAST dataset due to the more complex pore network of the sample consisting of much smaller pore sizes, even at a larger voxel size. However, U-Net++ and Attention U-Net are deeper and more complex models that were better able to generalize on the PAST dataset and yield better performance. Conversely, U-Net outperformed the other two models when applied on the MCAV_SCTLD2 dataset due to its simpler architecture.

With higher resolution data, the richer low-level details may suffice for good segmentations without the need for attention mechanisms or nested skip pathways. U-Net, while overfitting on other datasets, did not overfit as severely on the MCAV_SCTLD2 dataset due to the finer-grained details of the image data. It is important to note that patch sizes were not scaled with different voxel sizes. MCAV_SCTLD2 had the highest resolution, but the input image dimensions were not standardized, so the models were essentially fed smaller physical regions of each sample. For models like U-Net++ and Attention U-Net, which rely on contextual information and large receptive fields, this would be reflected in lower performance.

Nevertheless, these two datasets were included to test the performance of these models on unseen data with different characteristics than the training data and determine their ability to generalize across diverse data. Overall, the models proved to have good performance for this image segmentation task. Despite U-Net++ and Attention U-Net outperforming the standard U-Net model, U-Net may still prove to be useful for exploratory analysis but not necessarily for complex segmentations. Selecting the best model for predicting the negative class (pore) is specifically crucial for this porosity analysis. When also factoring in training times, Attention U-Net proved to be the most precise, robust and efficient model for most datasets, especially for applications where false positives should be avoided. Attention U-Net exhibited more consistency and generalizability across datasets compared to U-Net++ and may be the preferred model for tasks requiring computational simplicity and shorter training times.

To further verify these metrics with respect to performance, two-way ANOVA and Tukey's HSD tests were conducted. The two-way ANOVA test examines the effects of choice of model and dataset on performance. ANOVA results revealed that the choice of model had a highly statistically significant effect on model performance (Table 5). Similarly, the same posed true for the choice of dataset, which was expected given the diversity of properties of all the micro-CT datasets. Tukey's HSD pairwise comparisons provided insight into the statistical significance of mean differences in accuracies between each model (Table 6) where the accuracy is the difference between the deep learning model and the ground truth. As expected, the mean differences of both U-Net++ and Attention U-Net were statistically significantly higher than that of U-Net. Moreover, Attention U-Net had a slightly higher mean accuracy than U-Net++, but otherwise, differences between the two models were not statistically significant. In other words, based on accuracies per slice, U-Net++ and Attention U-Net are not statistically different. This implies that both models had comparable performances based on accuracies, including other performance metrics other than accuracy, which may have revealed statistical differences between the two. However, Attention U-Net holds an advantage of computational efficiency compared to U-Net++. Nonetheless, all models were further evaluated with respect to their subsequent skeletal porosity, density and thickness calculations and compared with their ground truth-derived counterparts.

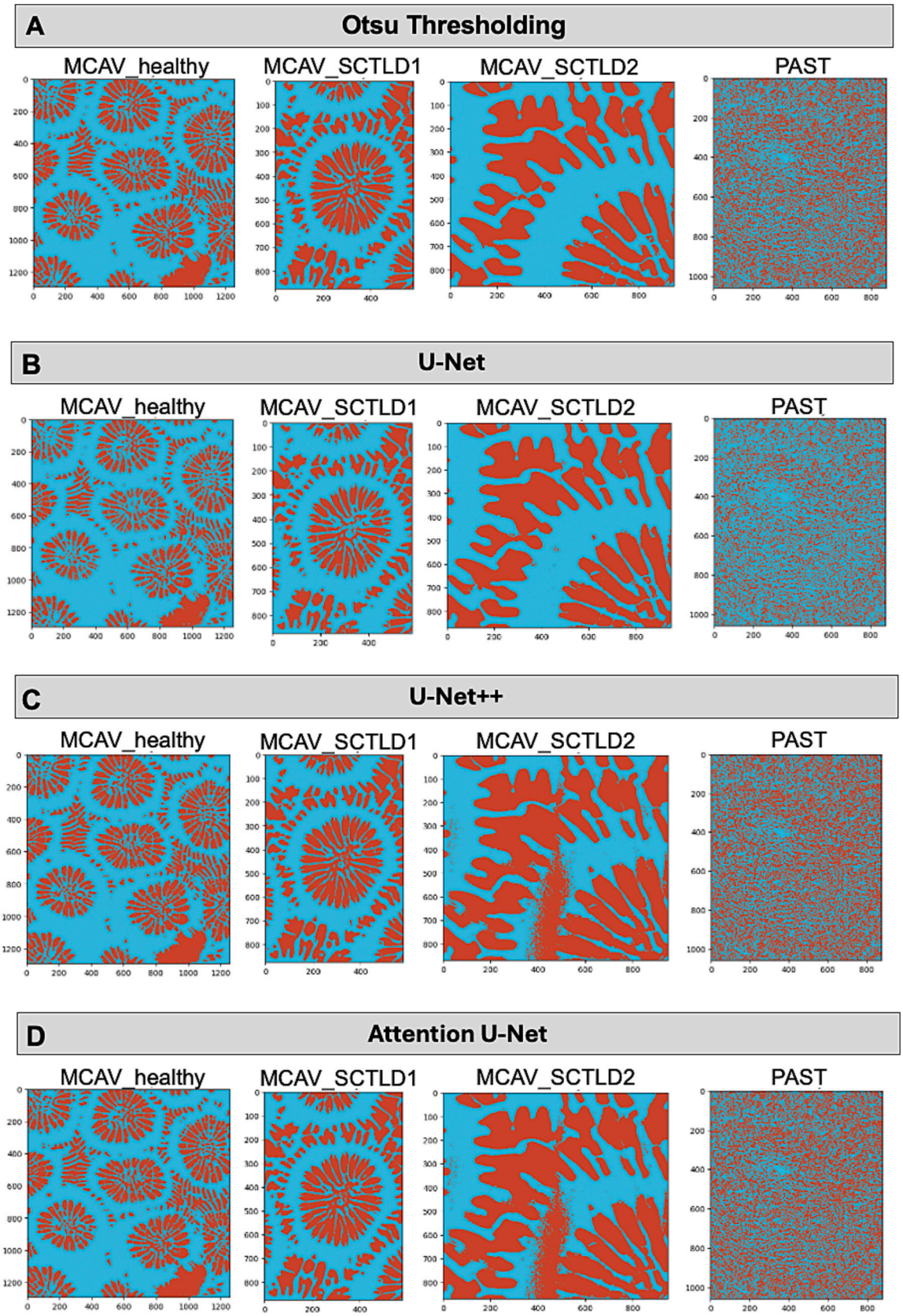

Fig. 6. Representative labeled image slices from all datasets produced from the (A) Otsu Thresholding method (ground truth), (B) U-Net, (C) U-Net++, and (D) Attention U-Net. Scales: A, B 1 px = 15.14 μm; C 1 px = 5.51 μm; D 1 px = 17.46 μm.

Table 5
Two-way ANOVA summary.

Source of variation	Sum of squares	df	F-statistic	p-value (significance*)
Model	2.1244	2.0	1613.1434	0.00E + 00***
Dataset	2.6730	3.0	1353.1505	0.00E + 00***
Residuals	4.5744	6947.0	–	–

*[***: p-value < 0.001 (highly significant)].

Table 6
Tukey's pairwise comparison summary.

Model 1	Model 2	Mean Diff (Accuracy)	95% Confidence interval	Adjusted p-value	Reject?
Attention U-Net	U-Net	−0.0372	[−0.0394, −0.0349]	0.0	True
Attention U-Net	U-Net++	−0.0002	[−0.0024, 0.0021]	0.9819	False
U-Net	U-Net++	0.0370	[0.0348, 0.0392]	0.0	True

3.2. Porosity and density analyses

Analysis of porosity and bulk density of all samples was performed using the segmented images from all predicted and ground truth segmentations. Mapping skeletal densities of corals using micro-CT can provide a better understanding of both species-dependent growth strategies and parameters in the context of pathogenesis from disease or paleoclimate reconstruction (Li et al., 2021; Williams et al., 2024). The distributions of porosities and bulk densities based on Attention U-Net segmentation across the depth of each sample were visualized (Fig. S2). Differences in porosity and density growth patterns can be observed for each sample. For example, MCAV_healthy shows a steady increase in porosity and decrease in density from the bottom to the top of the sample. Overall, the range of skeletal density values of around 1.5 to 1.7 g/cm^3 aligns with previous studies of coral density computations from micro-CT of the *Montastraea* genus (Bosscher, 1993). PAST exhibits a sharp increase bulk density close to the basal plate that quickly decreases and stabilizes around 4 mm. The porosity distribution of the PAST dataset matches closely with other studies of *P. astreoides,* with a positively skewed porosity curve with respect to its vertical profile and around 50–55% microporosity values (Uribe et al., 2025). The SCTLD samples show similar fluctuating but overall increasing porosities from bottom to top of the sample. A comparison of mean porosity and bulk density values derived from each model for all datasets with ground truth-derived values was performed to further evaluate the models for more meaningful biological metrics (Table 7). For example, the average bulk density of the MCAV_healthy dataset from U-Net segmentation is higher than that of the ground truth (Otsu) segmentation. Conversely, the average bulk density for this dataset from the U-Net++ and Attention U-Net are lower than that of the ground truth. This correlates with the larger FPR from the U-Net and the larger FNR for the U-Net++ and Attention U-Net models for MCAV_healthy. A similar trend is seen with all other models and datasets, where a larger density correlates with a larger FPR in evaluation because the model misclassifies pores as skeleton. This trend is opposite for average porosity, the negative class. Nonetheless, these results reveal that average porosity and bulk density values from Attention U-Net segmentation are similar to the ground truth for almost all datasets, except for MCAV_SCTLD2. Overall, this demonstrates how any misclassifications in segmentation by a model can trickle down to subsequent computations and that thorough model performance evaluations can help mitigate cascading errors. The SCTLD samples show different distributions. MCAV_SCTLD1 exhibits a fluctuating distribution of porosity and bulk density.

MCAV_SCTLD2 starts at a low porosity which increases to almost 58% porosity at 0.6 mm. The higher porosity for this sample compared to the others, which are around 35–50% may be due to the segmentation performance of Attention U-Net. Further investigation revealed that the image slices corresponding to a depth of around 0.6 mm show many mislabeled pixels as pores that are truly skeleton. This would explain this increased porosity in this region.

3.3. Skeletal thickness analysis

These segmentations were not only useful for porosity studies based on the voided space class but were also used to leverage the skeletal class for microscale thickness analyses. Thickness meshes were derived and visualized from the Attention U-Net skeletal segmentation class to generate false-colored 3D reconstructions that visualize local thickness values between boundary points for the MCAV_healthy, PAST, and MCAV_SCTLD1 samples (Fig. 7). Both *M. cavernosa* samples revealed similar thickness distributions, with lower uniform thicknesses within the septal region of a corallite, followed by higher thickness in the thecal

Table 7
Descriptive statistics and One-Way ANOVA results for slice-wise porosity and bulk density values computed for all datasets from each model and ground truth segmented labels.

Dataset	Segmentation method	Mean bulk density (g cm^{-1})	Mean porosity	Count (n)	F statistic	p-value (significance*)
MCAV_healthy	Otsu (ground truth)	1.817 ± 0.050	0.382 ± 0.017	536	1859.721	0.00E + 00***
	U-Net	1.976 ± 0.048	0.328 ± 0.016			
	U-Net++	1.779 ± 0.051	0.395 ± 0.017			
	Attention U-Net	1.779 ± 0.051	0.395 ± 0.017			
MCAV_SCTLD1	Otsu (ground truth)	1.722 ± 0.083	0.414 ± 0.028	367	456.553	2.40E-209***
	U-Net	1.893 ± 0.089	0.356 ± 0.030			
	U-Net++	1.699 ± 0.082	0.422 ± 0.028			
	Attention U-Net	1.699 ± 0.082	0.422 ± 0.028			
MCAV_SCTLD2	Otsu (ground truth)	1.657 ± 0.059	0.436 ± 0.020	175	965.157	1.90E-247***
	U-Net	1.604 ± 0.063	0.454 ± 0.021			
	U-Net++	1.344 ± 0.079	0.543 ± 0.027			
	Attention U-Net	1.348 ± 0.079	0.542 ± 0.027			
PAST	Otsu (ground truth)	1.603 ± 0.113	0.455 ± 0.038	447	1893.865	0.00E + 00***
	U-Net	1.939 ± 0.144	0.341 ± 0.049			
	U-Net++	1.440 ± 0.097	0.510 ± 0.033			
	Attention U-Net	1.440 ± 0.097	0.510 ± 0.033			

*[***: p-value < 0.001 (highly significant)].

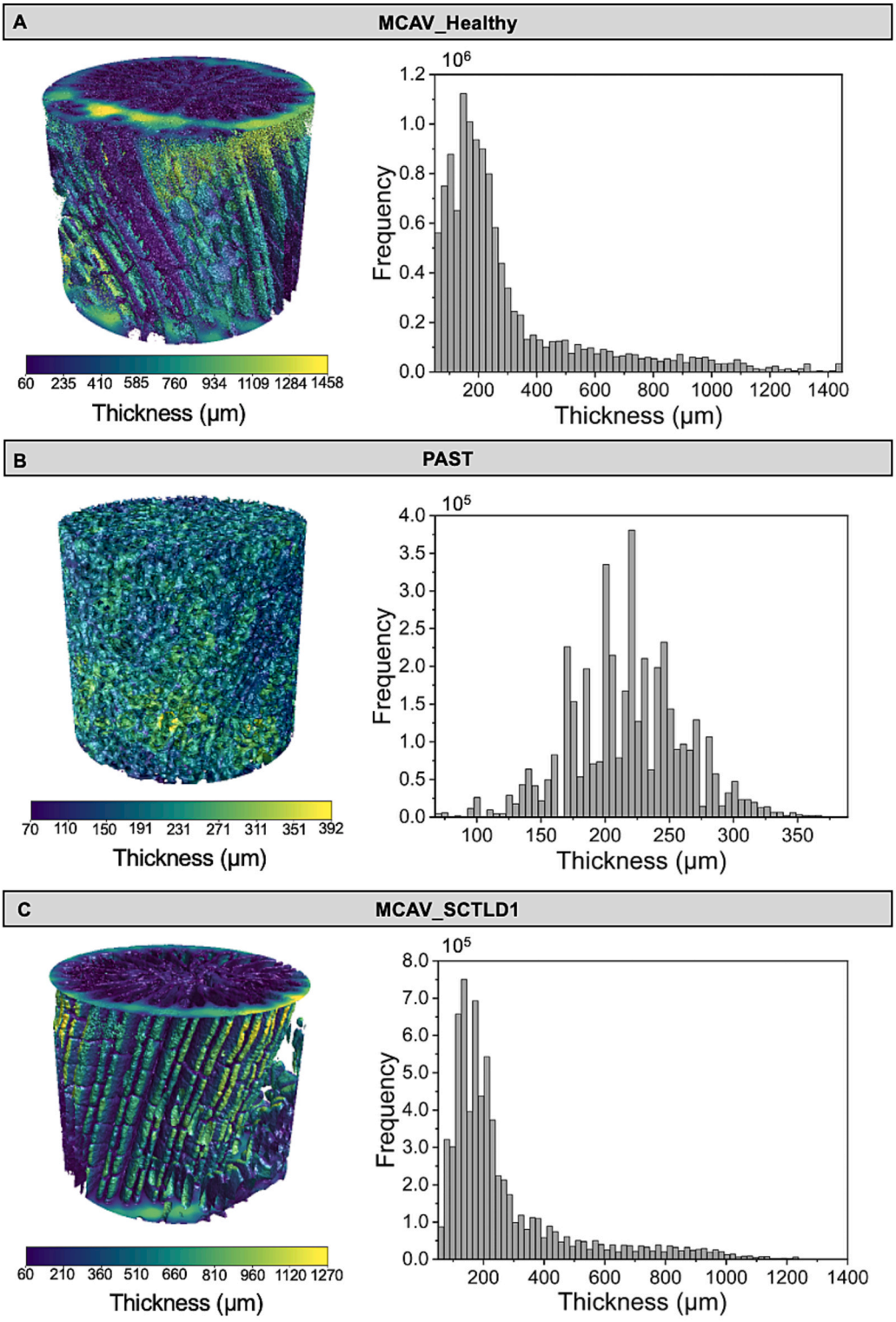

Fig. 7. 3D thickness meshes (left) and thickness value histograms (right) of skeleton class from Attention U-Net segmentations for (A) MCAV_healthy, (B) PAST and (C) MCAV_SCTLD2 samples.

region. This translates to positively skewed distributions, with predominantly small thicknesses of the corallites compared to larger thickness values from the less prominent thecal regions. Nevertheless, MCAV_healthy exhibited higher thickness values in this region from 1109 µm to 1458 µm compared to MCAV-SCTLD1, which showed values from 960 µm to 1270 µm. Contrastingly, PAST had a different thickness distribution mainly in the range of 110 µm to 351 µm, showing a normalized distribution compared to the *M. cavernosa* samples. In addition, the thickness patterns across the skeleton revealed scattered circular regions of higher thickness surrounded by areas of lower thickness. Furthermore, the mean thickness values across the regions of interest from each dataset were compared to the ground truth-derived values (Table S1). Amongst all the models, Attention U-Net achieved the closest thickness values to the ground truth ones across all three

datasets employed. These results elucidate aspects of coral growth in the context of disease and species-dependent growth patterns.

4. Conclusion

X-ray microcomputed tomography enables non-invasive structural characterization of biomaterials and biomineralized tissues across length scales, ranging from whole body imaging to nanoscale building blocks. Recent developments in semantic segmentation based on convolutional neural network models are poised to transform the quantitative analysis of large 3D tomography datasets, leading to optimized computational efficiency, accuracy, and generalizability. Deep learning image segmentation offers unique benefits in the morphological study of X-ray sensitive biological materials with complex micro- and nanostructures that suffer from poor contrast-to-noise ratios, paving the way for low-dose and time-resolved imaging in life sciences. Streamlined data processing can significantly reduce the time for analyzing large and complex tomography datasets. This work proposed a workflow for evaluating a series of U-Net models (U-Net, U-Net++, Attention U-Net) for semantic segmentation of micro-CT images of coral skeletons for porosity, density and local thickness analyses. Using *Dragonfly*, the models were trained using labeled images with two classes: pore and skeleton. The models were then tested on four distinct datasets: MCAV_healthy, MCAV_SCLTD1, MCAV_SCLD2, and PAST. Performance evaluations using various metrics and subsequent ANOVA and HSD tests revealed that Attention U-Net and U-Net++ were the top performing models. Attention U-Net was determined to be the best model for this application due to the highest performance in predicting the negative class (pores), its computational efficiency, and its generalizability on data from a different species with a more complex pore network. Porosities and bulk densities were computed and used to analyze the distributions for each sample, revealing differences in pore networks between species and between healthy and SCTLD-afflicted corals. Overall, this work provides a framework for leveraging sophisticated deep learning models for semantic segmentations of micro-CT data, specifically of biomineral systems like corals.

Nonetheless, a limitation of the present work is the non-standardized patch size construction in the CNN architecture resulting from different voxel sizes of the micro-CT scans. Prior studies have shown that CNN-based segmentations are sensitive to voxel-size heterogeneity, so future work should incorporate standardized voxel dimensions through acquisition settings (Çiçek et al., 2016) or voxel resampling (binning) (Isensee et al., 2021) to reduce the variability in model performance. The systematic analysis of common deep learning image segmentation approaches emphasized accuracy limitations that led to the mislabeling of pore or skeleton in datasets that starkly differed from the training data. Moreover, while the training sets were representative of coralline skeletal microstructures, the limited sample size and diversity restrict the models' abilities to learn and capture the biological variability across species and imaging parameters. Thus, setting aside more training data with high diversity would be essential to address any challenges in cross-system variability and improve accuracy and robustness of the deep-learning imaging approach (Greenspan et al., 2016; Maier et al., 2019). Another hurdle is the limited number of replicates and natural variability among biological samples.

CRediT authorship contribution statement

Alejandra Coronel-Zegarra: Writing – original draft, Visualization, Investigation, Formal analysis. **Jamie L. Knaub:** Writing – review & editing, Formal analysis, Data curation. **Vivian Merk:** Writing – review & editing, Supervision, Methodology, Funding acquisition, Conceptualization. **Abhijit Pandya:** Writing – review & editing, Validation, Supervision, Investigation, Conceptualization.

Declaration of competing interest

The authors declare that they have no known competing financial interests or personal relationships that could have appeared to influence the work reported in this paper.

Acknowledgements

V.M. is grateful to the National Science Foundation (DMR-2137663, Division of Materials Research) for partial financial support. A.C.Z. thanks the NSF NRT-HDR: Graduate Traineeship in Data Science Technologies and Applications program for support. This publication is based upon work partially supported by the National Science Foundation (DGE-2021585). Any opinions, findings, and conclusions or recommendations expressed in this material are those of the authors and do not necessarily reflect the views of the NSF. We thank FAU's College of Engineering and Computer Science (COECS) and I-SENSE for joint seed funding to V.M. and J.V. This work was produced in part using the Bruker SkyScan 1173 micro-CT system in the Berlin Family Bioimaging Lab at the FAU Lab Schools Marcus Research and Innovation Center (RRID:SCR_023805). Dr. Joshua Voss and Ashley Carreiro (Department of Biology, Harbor Branch Oceanographic Institute, Florida Atlantic University) are acknowledged for field-sampling coral skeletons under permit SAL-23-1702-SRP issued by the Florida Fish and Wildlife Conservation Commission.

Appendix A. Supplementary data

Supplementary data to this article can be found online at https://doi.org/10.1016/j.jsb.2026.108313.

Data availability

Data will be made available on request.

References

Alvarez-Filip, L., González-Barrios, F.J., Pérez-Cervantes, E., Molina-Hernández, A., Estrada-Saldívar, N., 2022. Stony coral tissue loss disease decimated Caribbean coral populations and reshaped reef functionality. Commun. Biol. 5 (1), 440. https://doi.org/10.1038/s42003-022-03398-6.

Andersson, E.R., Stewart, J.A., Work, T.M., Woodley, C.M., Schock, T.B., Day, R.D., 2020. Morphological, elemental, and boron isotopic insights into pathophysiology of diseased coral growth anomalies. Sci. Rep. 10 (1), 8252. https://doi.org/10.1038/s41598-020-65118-6.

Bosscher, H., 1993. Computerized tomography and skeletal density of coral skeletons. Coral Reefs 12 (2), 97–103. https://doi.org/10.1007/BF00302109.

Çiçek, Ö., Abdulkadir, A., Lienkamp, S.S., Brox, T., Ronneberger, O., 2016. 3D U-Net: learning dense volumetric segmentation from sparse annotation. *International Conference on Medical Image Computing and Computer-Assisted Intervention*, 424–432.

Cohen, D.J., Cheng, A., Sahingur, K., Clohessy, R.M., Hopkins, L.B., Boyan, B.D., Schwartz, Z., 2017. Performance of laser sintered Ti-6Al-4V implants with bone-inspired porosity and micro/nanoscale surface roughness in the rabbit femur. Biomed. Mater. (Bristol) 12 (2). https://doi.org/10.1088/1748-605X/aa6810.

Comet Technologies Canada Inc. (n.d.). *Dragonfly* (2024.1).

Dai, W., Fu, C., Raytcheva, D., Flanagan, J., Khant, H.A., Liu, X., Rochat, R.H., Haase-Pettingell, C., Piret, J., Ludtke, S.J., Nagayama, K., Schmid, M.F., King, J.A., Chiu, W., 2013. Visualizing virus assembly intermediates inside marine cyanobacteria. Nature 502 (7473), 707–710. https://doi.org/10.1038/nature12604.

Darrow, M.C., Sergeeva, O.A., Isas, J.M., Galaz-Montoya, J.G., King, J.A., Langen, R., Schmid, M.F., Chiu, W., 2015. Structural mechanisms of mutant huntingtin aggregation suppression by the synthetic chaperonin-like CCT5 complex explained by cryoelectron tomography. J. Biol. Chem. 290 (28), 17451–17461. https://doi.org/10.1074/jbc.M115.655373.

Davydzenka, T., Sinclair, D., Chawla, N., Tahmasebi, P., 2022. Deep-layers-assisted machine learning for accurate image segmentation of complex materials. Mater. Charact. 192, 112175. https://doi.org/10.1016/j.matchar.2022.112175.

Domart-Coulon, I.J., Traylor-Knowles, N., Peters, E., Elbert, D., Downs, C.A., Price, K., Stubbs, J., McLaughlin, S., Cox, E., Aeby, G., Brown, P.R., Ostrander, G.K., 2006. Comprehensive characterization of skeletal tissue growth anomalies of the finger coral *Porites compressa*. Coral Reefs 25 (4), 531–543. https://doi.org/10.1007/s00338-006-0133-6.

Duke, E.M.H., Darrow, M.C., Luengo, I., Basham, M., Spink, M.C., Irvine, S., French, A.P., Ashton, A.W., 2017. Volume segmentation and analysis of biological materials using

SuRVoS (super-region volume segmentation) workbench. J. Vis. Exp. 2017 (126). https://doi.org/10.3791/56162.
Dursun, T., Soutis, C., 2014. Recent developments in advanced aircraft aluminium alloys. Mater. Des. 1980–2015 (56), 862–871. https://doi.org/10.1016/j.matdes.2013.12.002.
Edie, S.M., Collins, K.S., Jablonski, D., 2023. High-throughput micro-CT scanning and deep learning segmentation workflow for analyses of shelly invertebrates and their fossils: examples from marine Bivalvia. Front. Ecol. Evol. 11. https://doi.org/10.3389/fevo.2023.1127756.
Fouke, K.W., Trop, J.M., Sivaguru, M., 2021. Changes in coral skeleton growth recorded by density band stratigraphy, crystalline structure, and hiatuses. Front. Mar. Sci. 8. https://doi.org/10.3389/fmars.2021.725122.
Fukushima, K., 1980. Neocognitron: a self-organizing neural network model for a mechanism of pattern recognition unaffected by shift in position. Biol. Cybern. 36 (4), 193–202. https://doi.org/10.1007/BF00344251.
Furat, O., Wang, M., Neumann, M., Petrich, L., Weber, M., Krill, C.E., Schmidt, V., 2019. Machine learning techniques for the segmentation of tomographic image data of functional materials. Front. Mater. 6. https://doi.org/10.3389/fmats.2019.00145.
Greenspan, H., van Ginneken, B., Summers, R.M., 2016. Guest editorial deep learning in medical imaging: overview and future promise of an exciting new technique. IEEE Trans. Med. Imaging 35 (5), 1153–1159. https://doi.org/10.1109/TMI.2016.2553401.
Hu, J., Shi, Y.N., Sauvage, X., Sha, G., Lu, K., 2017. Grain boundary stability governs hardening and softening in extremely fine nanograined metals. Science 355 (6331), 1292–1296. https://doi.org/10.1126/science.aal5166.
Isensee, F., Jaeger, P.F., Kohl, S.A.A., Petersen, J., Maier-Hein, K.H., 2021. nnU-Net: a self-configuring method for deep learning-based biomedical image segmentation. Nat. Methods 18 (2), 203–211. https://doi.org/10.1038/s41592-020-01008-z.
Lecun, Y., Bottou, L., Bengio, Y., Haffner, P., 1998. Gradient-based learning applied to document recognition. Proc. IEEE 86 (11), 2278–2324. https://doi.org/10.1109/5.726791.
Li, Y., Liao, X., Bi, K., Han, T., Chen, J., Lu, J., He, C., Lu, Z., 2021. Micro-CT reconstruction reveals the colony pattern regulations of four dominant reef-building corals. Ecol. Evol. 11 (22), 16266–16279. https://doi.org/10.1002/ece3.8308.
Lough, J.M., Cooper, T.F., 2011. New insights from coral growth band studies in an era of rapid environmental change. Earth Sci. Rev. 108 (3), 170–184. https://doi.org/10.1016/j.earscirev.2011.07.001.
Maier, A., Syben, C., Lasser, T., Riess, C., 2019. A gentle introduction to deep learning in medical image processing. Zeitschrift Für Medizinische Physik 29 (2), 86–101. https://doi.org/10.1016/j.zemedi.2018.12.003.
Maire, E., Withers, P.J., 2014. Quantitative X-ray tomography. Int. Mater. Rev. 59 (1), 1–43. https://doi.org/10.1179/1743280413Y.0000000023.
Minaee, S., Boykov, Y., Porikli, F., Plaza, A., Kehtarnavaz, N., Terzopoulos, D., 2022. Image segmentation using deep learning: a survey. IEEE Trans. Pattern Anal. Mach. Intell. 44 (7), 3523–3542. https://doi.org/10.1109/TPAMI.2021.3059968.
Oktay, O., Schlemper, J., Folgoc, L. Le, Lee, M., Heinrich, M., Misawa, K., Mori, K., McDonagh, S., Hammerla, N. Y., Kainz, B., Glocker, B., Rueckert, D., 2018. *Attention U-Net: Learning Where to Look for the Pancreas*. http://arxiv.org/abs/1804.03999.
Otsu, N., 1979. A threshold selection method from gray-level histograms. IEEE Trans. Syst. Man Cybern. 9 (1), 62–66. https://doi.org/10.1109/TSMC.1979.4310076.
Papke, E., Carreiro, A., Dennison, C., Deutsch, J.M., Isma, L. M., Meiling, S.S., Rossin, A. M., Baker, A.C., Brandt, M.E., Garg, N., Holstein, D.M., Traylor-Knowles, N., Voss, J. D., Ushijima, B., 2023. Stony coral tissue loss disease: a review of emergence, impacts, etiology, diagnostics, and intervention. In *Frontiers in Marine Science* (Vol. 10). Frontiers Media SA. Doi:10.3389/fmars.2023.1321271.
Raja Somu, D., Cracchiolo, T., Longo, E., Greving, I., Merk, V., 2023. On stars and spikes: resolving the skeletal morphology of planktonic Acantharia using synchrotron X-ray nanotomography and deep learning image segmentation. Acta Biomater. 159, 74–82. https://doi.org/10.1016/j.actbio.2023.01.037.
Raja Somu, D., Soini, S.A., Briggs, A., Singh, K., Greving, I., Porter, M., Passerotti, M., Merk, V., 2025. A nanoscale view of the structure and deformation mechanism of mineralized shark vertebral cartilage. ACS Nano 19 (14), 14410–14421. https://doi.org/10.1021/acsnano.5c02004.
Reznikov, N., Buss, D.J., Provencher, B., McKee, M.D., Piché, N., 2020. Deep learning for 3D imaging and image analysis in biomineralization research. J. Struct. Biol. 212 (1), 107598. https://doi.org/10.1016/j.jsb.2020.107598.
Ronneberger, O., Fischer, P., Brox, T., 2015. *U-Net: Convolutional Networks for Biomedical Image Segmentation*. http://arxiv.org/abs/1505.04597.
Roslin, A., Marsh, M., Piché, N., Provencher, B., Mitchell, T.R., Onederra, I.A., Leonardi, C.R., 2022. Processing of micro-CT images of granodiorite rock samples using convolutional neural networks (CNN), part I: super-resolution enhancement using a 3D CNN. Miner. Eng. 188, 107748. https://doi.org/10.1016/j.mineng.2022.107748.
Rubio, J.E., Chakravarty, U.K. 2016, November 11. An Investigation of the Aerodynamic Performance of a Biomimetic Insect-Sized Wing for Micro Air Vehicles. *Volume 1: Advances in Aerospace Technology*. Doi:10.1115/IMECE2016-65303.
San, X., Gong, M., Wang, J., Ma, X., dos Reis, R., Smeets, P.J.M., Dravid, V.P., Hu, X., 2022. Uncovering the crystal defects within aragonite $CaCO_3$. Proc. Natl. Acad. Sci. 119 (14), e2122218119. https://doi.org/10.1073/pnas.2122218119.
Scucchia, F., Sauer, K., Fara, S., Mass, T., Zaslansky, P., 2025. 4D insights into coral biomineralization: effects of ocean acidification on the early skeleton development of a stony coral. Adv. Sci., e08585 https://doi.org/10.1002/advs.202508585.
Scucchia, F., Sauer, K., Zaslansky, P., Mass, T., 2022. Artificial intelligence as a tool to study the 3D skeletal architecture in newly settled coral recruits: insights into the effects of ocean acidification on coral biomineralization. J. Mar. Sci. Eng. 10 (3). https://doi.org/10.3390/jmse10030391.
Scucchia, F., Wong, K., Zaslansky, P., Putnam, H.M., Goodbody-Gringley, G., Mass, T., 2023. Morphological and genetic mechanisms underlying the plasticity of the coral *Porites astreoides* across depths in Bermuda. J. Struct. Biol. 215 (4), 108036. https://doi.org/10.1016/j.jsb.2023.108036.
Thompson, D.M., 2022. Environmental records from coral skeletons: a decade of novel insights and innovation. WIREs Clim. Change 13 (1), e745. https://doi.org/10.1002/wcc.745.
Uribe, E.S., Murgueitio, A., Gómez, C.E., Acosta, A., Sánchez, J.A., 2025. Endolithic algae influence the skeletal microstructure and porosity of reef-building corals. Sci. Rep. 15 (1), 26893. https://doi.org/10.1038/s41598-025-99374-1.
Vásárhelyi, L., Kónya, Z., Kukovecz, Á., Vajtai, R., 2020. Microcomputed tomography–based characterization of advanced materials: a review. Mater. Today Adv. 8, 100084. https://doi.org/10.1016/j.mtadv.2020.100084.
Vincent, J., Sheldrake, T., 2025. Micro-CT analysis reveals porosity driven growth banding in Caribbean coral *Siderastrea siderea*. Sci. Rep. 15 (1), 6063. https://doi.org/10.1038/s41598-025-90125-w.
Waibel, A., Hanazawa, T., Hinton, G., Shikano, K., Lang, K.J., 1989. Phoneme recognition using time-delay neural networks. IEEE Trans. Acoust. Speech Signal Process. 37 (3), 328–339. https://doi.org/10.1109/29.21701.
Wang, R., Lei, T., Cui, R., Zhang, B., Meng, H., Nandi, A.K., 2022. Medical image segmentation using deep learning: a survey. IET Image Proc. 16 (5), 1243–1267. https://doi.org/10.1049/ipr2.12419.
Wang, R., Stone, R.L., Kaelber, J.T., Rochat, R.H., Nick, A.M., Vijayan, K.V., Afshar-Kharghan, V., Schmid, M.F., Dong, J.-F., Sood, A.K., Chiu, W., 2015. Electron cryotomography reveals ultrastructure alterations in platelets from patients with ovarian cancer. Proc. Natl. Acad. Sci. USA 112 (46), 14266–14271. https://doi.org/10.1073/pnas.1518628112.
Williams, T.J., Basford, P.J., Katsamenis, O.L., Solan, M., Foster, G.L., Standish, C., Godbold, J.A., Archambault, P., 2024. Three-dimensional reconstruction of high latitude bamboo coral via X-ray microfocus computed tomography. Sci. Data 11 (1), 602. https://doi.org/10.1038/s41597-024-03396-9.
Zhang, R., Li, W., Jiao, Y., Paniagua, C., Ren, Y., Lu, H., 2023. Porosity evolution under increasing tension in wire-arc additively manufactured aluminum using in-situ micro-computed tomography and convolutional neural network. Scr. Mater. 225, 115172. https://doi.org/10.1016/j.scriptamat.2022.115172.
Zhong, S., Yin, Y., Liang, X., Deng, Q., 2024. Aragonite and its composites: preparations, properties and applications. Eur. J. Inorg. Chem. 27 (20), e202300733. https://doi.org/10.1002/ejic.202300733.
Zhou, Z., Siddiquee, M.M.R., Tajbakhsh, N., Liang, J., 2018. *UNet++: A Nested U-Net Architecture for Medical Image Segmentation*. http://arxiv.org/abs/1807.10165.